Bioelectromagnetics 25:285–295 (2004)

Metallic Electrodes and Leads in Simultaneous EEG-MRI: Specific Absorption Rate (SAR) Simulation Studies

Leonardo M. Angelone,* Andreas Potthast, Florent Segonne, Sunao Iwaki, John W. Belliveau, and Giorgio Bonmassar

MGH/MIT/HMS Athinoula A. Martinos Center for Functional Imaging, Charlestown, Massachusetts

The purpose of this study was to investigate the changes in specific absorption rate (SAR) in human-head tissues while using nonmagnetic metallic electroencephalography (EEG) electrodes and leads during magnetic resonance imaging (MRI). A realistic, high resolution (1 mm^3) head model from individual MRI data was adopted to describe accurately thin tissues, such as bone marrow and skin. The RF power dissipated in the human head was evaluated using the FDTD algorithm. Both surface and bird cage coils were used. The following numbers of EEG electrodes/leads were considered: 16, 31, 62, and 124. Simulations were performed at 128 and 300 MHz. The difference in SAR between the electrodes/leads and no-electrodes conditions was greater with the bird cage coil than with the surface coil. The peak 1 g averaged SAR values were highest at 124 electrodes, increasing to as much as two orders of magnitude ($\times$172.3) at 300 MHz compared to the original value. At 300 MHz, there was a fourfold ($\times$3.6) increase of SAR averaged over the bone marrow, and a sevenfold ($\times$7.4) increase in the skin. At 128 MHz, there was a fivefold ($\times$5.6) increase of whole head SAR. Head models were obtained from two different subjects, with an inter-subject whole head SAR variability of 3%. Bioelectromagnetics 25:285–295, 2004.

Key words: induced currents; RF coils; numerical dosimetry; FDTD; MRI; SAR

INTRODUCTION

One of the important challenges of brain imaging is to model the sources of brain activity during different tasks, such as visual, auditory, or motor tasks. Currently, there is no single noninvasive technology that can provide the high spatio-temporal resolution needed to study this brain activity. This problem has been addressed through multi-modal integration of different modalities, such as electroencephalography (EEG) and functional magnetic resonance imaging (fMRI), which offer high temporal and spatial resolution, respectively.

Simultaneous recordings of hemodynamic and electrophysiological changes have become more common in clinical research [Hill et al., 1995; Huang-Hellinger et al., 1995; Bonmassar et al., 1999, 2001; Chiappa et al., 1999; Krakow et al., 2000; Lemieux et al., 2001]. However, these raise safety issues, since the use of electrodes/leads in an MRI environment is in many respects similar to the presence of metallic implants in an MRI environment. Previous studies have analyzed the safety issues associated with metallic implants and MRI [Gangarosa et al., 1987; Buchli et al., 1988; Kanal et al., 1990; Gigli et al., 1992; Schaefer, 1992, 1998; Chou et al., 1995, 1997; Fagan et al., 1995; Shellock et al., 1995; Nelson et al., 1997; Furse and Gandhi, 1998; Youssefzadeh et al., 1998; Shellock, 1999, 2000, 2001; Edwards et al., 2000; Schaefer et al., 2000; Ho, 2001; Pruefer et al., 2001; Yeung et al., 2002] and simultaneous EEG–MRI recording [Lemieux et al., 1997; Lazeyras et al., 2001; Bonmassar et al., 2002]. These studies have shown that, in cases where heating of tissue occurred, heating is a function of dimensions, orientation, shape, and location of the implant in the patient. Furthermore, in the case of metallic wire, the location of the heating in the tissue is usually concentrated in a small volumetric area near the tip

Grant sponsor: Whitaker Foundation; Grant number: RG-99-0408.

*Correspondence to: Leonardo M. Angelone, MGH/MIT/HMS Athinoula A. Martinos Center for Functional Imaging, Building 149, 13th Street, Charlestown, MA 02129.
E-mail: angelone@nmr.mgh.harvard.edu

Received for review 18 March 2003; Final revision received 10 October 2003

DOI 10.1002/bem.10198
Published online in Wiley InterScience (www.interscience.wiley.com).

[Ho, 2001]. The risk of heating due to the presence of induced currents on the leads and in their proximity may be reduced with resistive leads technology [Chou and Guy, 1979; Hill et al., 1995; Huang-Hellinger et al., 1995; Bonmassar et al., 1999, 2001; Chiappa et al., 1999; Goldman et al., 2000; Krakow et al., 2000; Van Audekerkea et al., 2000; Lemieux et al., 2001]. However, a number of laboratories around the world still use nonmagnetic metallic leads and conventional EEG electrodes during simultaneous EEG–MRI recording [Ives et al., 1993, 1995; Jackson, 1994; Kohno et al., 1995; Sijbers et al., 1999; Kruggel et al., 2000, 2001; Portas et al., 2000; Benar et al., 2002; Christmann et al., 2002; Horovitz et al., 2002; Jager et al., 2002; Matsuda et al., 2002]. Hence, we modeled the EEG electrodes and leads as perfect electric conductors (PEC).

Previous studies used $2 \times 2 \times 2.5$ mm^3 resolution for their head model [Jin et al., 1996; Jin, 1999; Collins and Smith, 2001a,b]. However, in order to study very thin tissues close to the EEG electrodes, such as bone marrow and skin, we increased the resolution of the head model to $1 \times 1 \times 1$ mm^3. Furthermore, the low dimension of the cells (1/500 to 1/1000 of the wavelength) improves the geometrical modeling of small and curved structures and reduces the issues of the staircased model, as suggested by previous studies [Holland, 1993; Railton and Schneider, 1999].

The current tendency with advanced MRI, such as fMRI, is to increase the signal-to-noise ratio (SNR) and the spatial resolution by increasing the static field B_0. Higher RF (B_1) frequency systems are needed at higher B_0 because of the linear relation between Larmor frequency and B_0 field strength [Collins and Smith, 2001b]. Simulations were performed at 128 and 300 MHz, corresponding to 3 and 7 T MRI systems, respectively, to evaluate the effects of frequency increase with the EEG electrode/lead model. One open issue was whether or not the electromagnetic resonance inside the head could generate a local SAR maximum in the parenchymal tissues rather than on the skin.

MATERIALS AND METHODS

Subject Information

Two normal adult male volunteers participated in this study. Informed consent was obtained from each subject in accordance with Massachusetts General Hospital policies (IRB #1999-P-010946/1; MGH).

Head Model

Two high resolution head models were generated by applying a segmentation [Dale et al., 1999; Segonne et al., 2001] to the anatomical MRI data of two adult male subjects. The brain was segmented using a hybrid method combining watershed algorithms and deformable surface techniques. Using a three component mixture model, whose parameters were computed during the skull stripping process, the brain was segmented into cerebrospinal fluid (CSF), gray matter, and white matter. A deformable balloon-like template was then iteratively mapped onto the scalp boundary and the remaining tissues were classified as fat tissue, bone and cartilage, and skin. Bone marrow and eyes were later segmented by a threshold based method on the T1 weighted images, under the supervision of an expert radiologist.

The anatomical MRI for subject no. 1 was performed with a quadrature bird cage transmit/receive head coil on our 1.5 T scanner (General Electric, Milwaukee, WI). Three whole head acquisitions were collected with a T1 weighted three dimensional (3D)-SPGR sequence (TR/TE = 24/8 ms) with 124 slices, 1.3 mm thick (matrix size 256×192, FOV 256 mm). The individual acquisitions were motion corrected and averaged to increase gray/white matter contrast-to-noise ratio using MEDx software (Sensor Systems, Inc., Sterling, VA).

The anatomical MRI for subject no. 2 was performed with a quadrature bird cage transmit/receive head coil on our 3 T whole body Siemens Trio (Erlangen, Germany). Three whole head acquisitions were collected with a T1 weighted MPRAGE sequence (TR/TE = 2530/3.26 ms) with 128 slices, 1.3 mm thick (matrix size 256×192, FOV 256 mm).

Each cell of the head model was an isotropic voxel of dimension $1 \times 1 \times 1$ mm^3. The dimensions of the head model for subject no. 1 were 167 mm from left to right, 205 mm from back to front, and 236 mm high. The dimensions of the head model for subject no. 2 were 185 mm from left to right, 208 mm from back to front, and 228 mm high. The total number of Yee cells [Yee, 1966] for the head models was 4 395 536 for subject no. 1 and 4 582 477 for subject no. 2. Yee cells, containing six field components (Ex, Ey, Ez, Hx, Hy, and Hz, all offset by half a space step), are used in the FDTD algorithm for a 3D central difference approximation of Maxwell's curl equations, both in space and time. The total volume considered for both subjects, including the free space around the model, was $296 \times 296 \times 390$ mm^3. Absorbing boundary conditions of the "Liao" type were used for the FDTD calculation [Kunz and Luebbers, 1993].

Figure 1 shows the high resolution head model and an axial MRI image with the SAR levels of subject no. 1 superimposed onto it. The high resolution of the model is necessary to segment thin layers of tissues,

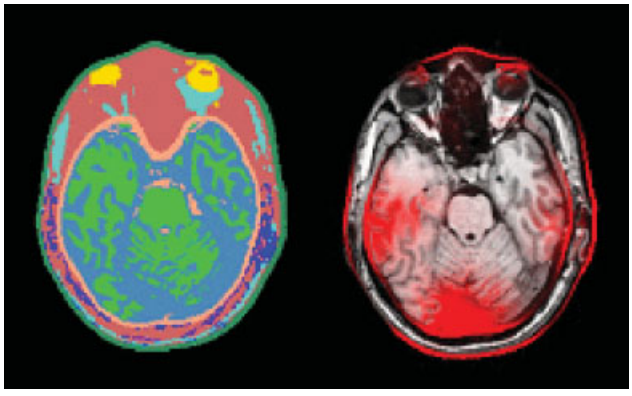

Fig. 1. High resolution head model (left; see caption of Fig. 2 for tissue color key) and axial MRI image with specific absorption rate (SAR) levels superimposed (right), for subject no. 1. Resolution of at least $1 \times 1 \times 1$ mm^3 is necessary in the segmentation of thin layers of tissues, such as skin and bone marrow.

such as skin and bone marrow. Eight different types of tissue (bone and cartilage, skin, CSF, white matter, gray matter, fat, bone marrow, and eyes) were distinguished and their physical properties selected according to the literature (see Table 1). The current version of the automatic segmentation software based on T1 weighted MRI data does not allow for discrimination of tissues other than those given, for example, blood, muscle, sclera, cornea, nerve, tongue, and cerebellum [Collins and Smith, 2001b]. Figure 2 shows the head models from two different subjects used in this study.

SAR Estimation

Specific absorption rate (SAR) is the variable typically used in dosimetry to quantify the tissue exposure to RF. SAR is defined as the time derivative of the incremental energy absorbed by (dissipated in) an incremental mass contained in a volume of a given density [NCRP, 1981; Chou et al., 1996], and is expressed in W/kg. The relation between SAR and the electrical induced field is [Jin, 1999; Yeung et al., 2002]

$$\mathrm{SAR} = \frac{\sigma_e}{2\rho}\left|\vec{E}\right|^2,$$

where σ_e (S/m) is the electric conductivity, ρ (kg/m^3) is the tissue density, and $\vec{E}$ (V/m) is the peak electric field intensity inside the tissue.

TABLE 1. Conductivity, Permittivity, and Density of the Tissues Used in the Head Model

Tissue	Density (kg/m^3)	128 MHz-3 T		300 MHz-7 T	
		σ (S/m)	ε_r	σ (S/m)	ε_r
Bone and cartilage	1850[a]	0.20[c]	30[c]	0.20[c]	20[c]
Skin	1100[a]	0.50[c]	70[c]	0.50[c]	45[c]
CSF	1060[a]	0.70[d]	103[d]	0.80[d]	100[d]
White matter	1030[a]	0.35[c]	50[c]	0.50[c]	40[c]
Grey matter	1030[a]	0.60[c]	80[c]	0.80[c]	60[c]
Fat	920[a]	0.03[c]	12[c]	0.04[c]	5[c]
Eyes tissue	1010[a]	1.00[c]	70[c]	0.98[c]	60[c]
Bone marrow	970[b]	0.19[c]	15[c]	0.20[c]	12[c]

CSF, cerebrospinal fluid.
[a]From Moneda et al. [2003].
[b]From Masumoto et al. [1997].
[c]From Gabriel et al. [1996a–c].
[d]From Jin [1999].

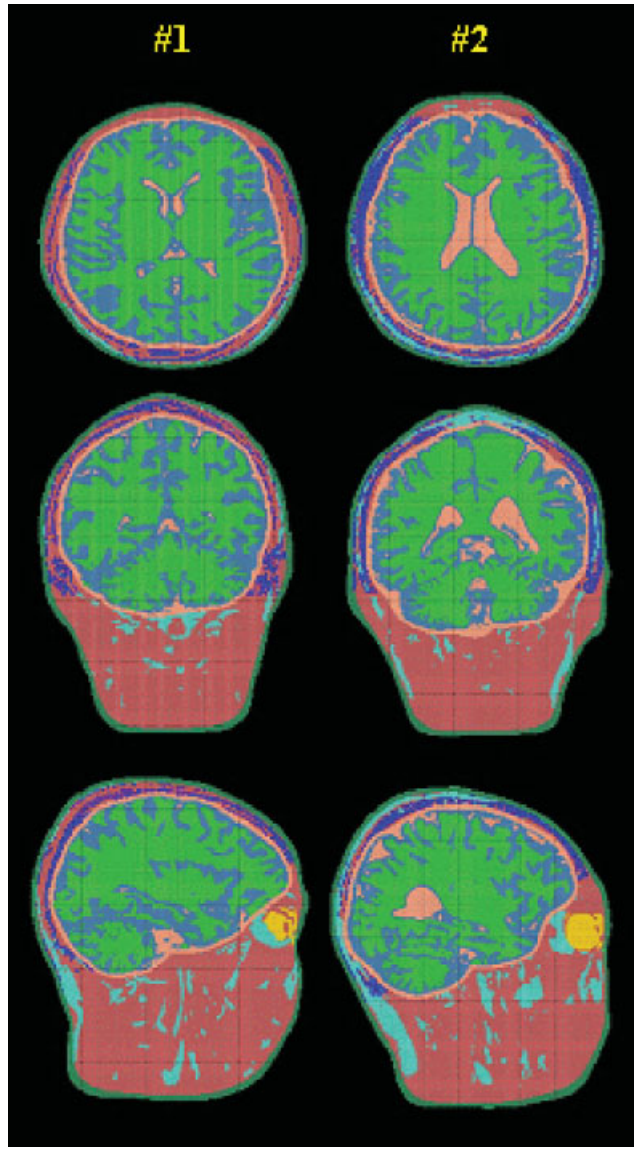

Fig. 2. Head models from two different subjects used in this study. Tissues are displayed as follows: bone and cartilage in pink; skin in dark green, cerebrospinal fluid (CSF) in light pink, white matter in green, gray matter in blue, fat in light blue, bone marrow in purple, and eyes in yellow.

The electric and magnetic fields and the SAR values were computed using the commercially available software XFDTD (REMCOM Co., State College, PA), based on the FDTD algorithm [Kunz and Luebbers, 1993; Taflove and Hagness, 2000]. Both whole head and peak 1 g averaged values of SAR were computed. The averaging calculations were computed according to the methods described in Kunz and Luebbers [1993]. Cubical spaces centered on a cell are formed and the mass and average SAR of the sample cubes are found. The size of the sample cubes increases in odd numbered steps to remain centered on the desired cell. The average number of cells for 1 g average in our head model was 731.3 for subject no. 1 and 769.86 for subject no. 2. The mass and average SAR value of each cube is saved and used to interpolate the average SAR values at 1 g. The interpolation is performed with two methods, polynomial fit and rational function fit, and the method with the lowest error is chosen. The sample cube must meet certain conditions to be considered valid: it may contain some nontissue cells, but will not contain an entire side or corner of nontissue cells. If the cube is found to be invalid, the averaging will stop for the center cell and move on the next cell. Some cells might not be the center of an average. However, these cells will often be part of an average cube for an adjacent cell.

Simulations were performed with two different coils (surface and bird cage coil), four different numbers of EEG electrodes/leads (16, 31, 62, and 124), and two frequencies (128 and 300 MHz). An Athlon MP2100 computer with 3.5 GB of RAM memory was used for the calculations. The computation time under Windows 2000 was approximately 36 h for 300 MHz and 100 h for 128 MHz; 20% less computation time was measured under Linux.

MRI Coils

SAR simulations were computed modeling two different RF coils (surface and bird cage coil) and two different frequencies (128 and 300 MHz).

The bird cage coil [Ho, 2001] was composed of 16 PEC rods (length 310 mm), closed by two PEC loops at each end (diameter 260 mm, thickness 1 mm), and placed symmetrically around the head [Jin, 1999]. A circular excitation was simulated, driving the current generators placed on the centers of the rods with 1 A peak-to-peak amplitude and a 22.5° phase-shift between any two adjacent generators.

The surface coil used was a circular perfect electrical conductor (PEC), ring-shaped and oriented in the XZ plane (coronal, coordinates as in Fig. 3) with a diameter of 140 mm and thickness of 1 mm. The current source, a sinusoidal generator of 1 A peak-to-peak amplitude with internal resistance of 50 Ω, was placed on the lowest point of the ring.

EEG Electrodes Cap

In our simulations, the EEG electrodes and leads were modeled with PEC [Bonmassar et al., 2002]. Different montages of EEG electrodes, i.e., different numbers of electrodes, were used in the simulations. The positions of the 124 electrodes and leads were digitized directly on the head of the subject with a Fastrack 3D digitizer (Polhemus, Colchester, VT) and Scan 4.2 software (Compumedics, El Paso, TX) on a nonmagnetic cap (Neuromag, Finland) [Virtanen et al., 1996]. One point for each electrode and four points for each wire were digitized, then imported into MATLAB (Mathworks Co., Natick, MA) and registered to the high resolution model. Figure 3, generated with the 3DSpaceDx software (Neurosoft–Compumedics, El Paso, TX), shows a 3D view of the position of the 128 electrodes on the head. The electrodes were in direct contact with the skin. Subsampling of the digitized electrode positions model was performed to include simulations with 62, 31, and 16 electrodes/leads. These decimations were performed by selecting one point from every two, four, and eight electrodes/leads, respectively, of the 124 electrode/lead model, which lead to uniform spatial sampling in all cases. The EEG electrodes were modeled as small cylinders (radius: 2 mm, height: 1 mm).

TABLE 2. Normalized Peak 1 g Averaged SAR Values Computed Using Surface and Bird Cage Coil, Without and With Electrodes/Leads

	Peak 1 g SAR values					
	128 MHz-3 T			300 MHz-7 T		
	No electrodes (W/kg)	124 electrode (W/kg)	Ratio electrode/ no electrode	No electrodes (W/kg)	124 electrode (W/kg)	Ratio electrode/ no electrode
Bird cage	0.36	22.30	61.62	0.13	21.89	172.32
Surface	2.33	36.63	15.71	2.33	36.32	15.57

All specific absorption rate (SAR) values are computed for an input power of 1 W.

TABLE 3. Normalized SAR Values Computed With Bird Cage Coil and Input Power of 1 W

	Bird cage (W/kg)						
	128 MHz-3 T		300 MHz-7 T				
	No electrodes	124 electrode	No electrodes	16 electrode	31 electrode	62 electrode	124 electrode
Whole head	0.05	0.28	0.03	0.07	0.07	0.07	0.09
Max 1 g averaged	0.36	22.30	0.13	20.43	15.65	15.86	21.89
Bone and cartilage	0.03	0.23	0.02	0.03	0.05	0.05	0.06
Skin	0.10	0.92	0.05	0.23	0.23	0.29	0.37
CSF	0.07	0.30	0.04	0.09	0.06	0.06	0.07
White matter	0.05	0.22	0.04	0.09	0.05	0.05	0.06
Grey matter	0.05	0.22	0.03	0.08	0.05	0.05	0.07
Fat	0.03	0.27	0.02	0.11	0.08	0.10	0.13
Eyes tissue	0.13	0.57	0.04	0.16	0.07	0.09	0.17
Bone marrow	0.04	0.40	0.03	0.06	0.09	0.11	0.11

Normalized whole head, peak 1 g averaged, and values averaged over each tissue are estimated for subject no. 1.

RESULTS

All of the SAR simulations indicated that the increase in the electrodes/leads versus no-electrodes condition was greater with the bird cage coil than with the surface coil (e.g., Table 2). Furthermore, the 124 electrode/lead model leads to higher peak 1 g averaged SAR values for both the bird cage coil and the surface coil (Tables 3 and 4).

With the electrode/lead model, we did not observe a higher peak value of SAR in the parenchymal tissues than on the skin (Tables 3 and 4). The cortical inflated representation [Dale and Sereno, 1993; Fischl et al., 1999] was used, distinguishing the sulci and the gyri of the cortex through the use of two shades of green (light for gyri and dark for sulci). SAR values were superimposed onto the MRI images with Freesurfer [2003] and displayed on the whole cortex with a color based scale (Figs. 4 and 5).

Effects of the EEG Montage

Previous studies have shown that a conductive wire structure alters the electric field distribution near a wire [Yeung et al., 2002]. Figure 6 illustrates the electric field distribution with bird cage and surface coils in four different cases: coil only, coil plus head, coil plus electrodes/leads, and coil plus head and electrodes/leads. The electric field produced by the bird cage coil is circularly symmetric. The electric field produced by the surface coil is axially symmetric. The electric field becomes less uniform and decreases in presence of

TABLE 4. Normalized SAR Values Computed With Surface Coil and Input Power of 1 W

	Surface (W/kg)						
	128 MHz-3 T		300 MHz-7 T				
	No electrodes	124 electrode	No electrodes	16 electrode	31 electrode	62 electrode	124 electrode
Whole head	0.28	0.17	0.24	0.18	0.17	0.16	0.17
Max 1 g averaged	2.33	36.63	2.33	24.06	27.86	20.13	36.32
Bone and cartilage	0.13	0.11	0.08	0.06	0.06	0.06	0.08
Skin	0.59	0.77	0.29	0.35	0.41	0.43	0.49
CSF	0.58	0.16	0.44	0.29	0.25	0.23	0.23
White matter	0.41	0.10	0.42	0.27	0.24	0.29	0.22
Grey matter	0.35	0.09	0.42	0.27	0.24	0.23	0.21
Fat	0.18	0.23	0.13	0.10	0.11	0.11	0.17
Eyes tissue	0.02	0.01	0.03	0.02	0.02	0.01	0.01
Bone marrow	0.42	0.47	0.28	0.23	0.23	0.24	0.37
Ratio posterior/ anterior (a.u.)	10.00	16.10	8.03	10.06	11.79	13.95	18.44

Normalized whole head, peak 1 g averaged, and values averaged over each tissue are estimated for subject no. 1. The last row of the surface coil table shows the ratio of total SAR values of posterior side of the head versus anterior side.

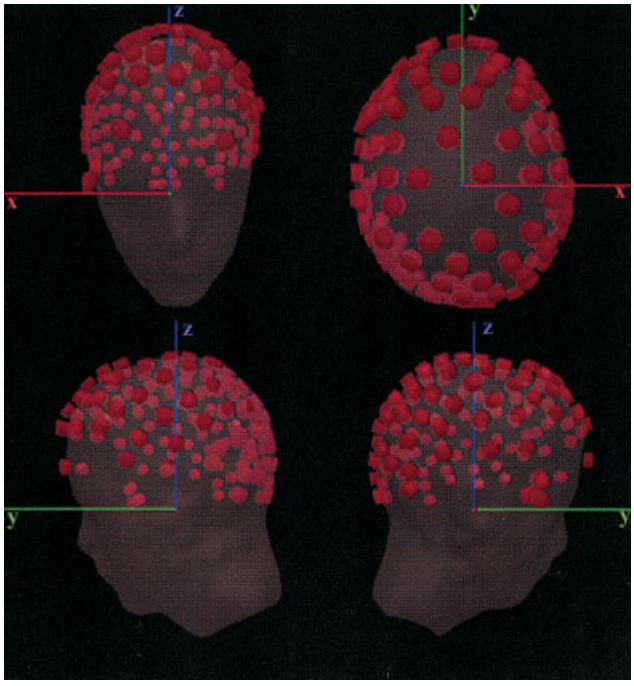

Fig. 3. Three dimensional (3D) view of the electroencephalography (EEG) electrodes directly digitized on the subject's head with reference axes superimposed (x in red, y in green, z in blue).

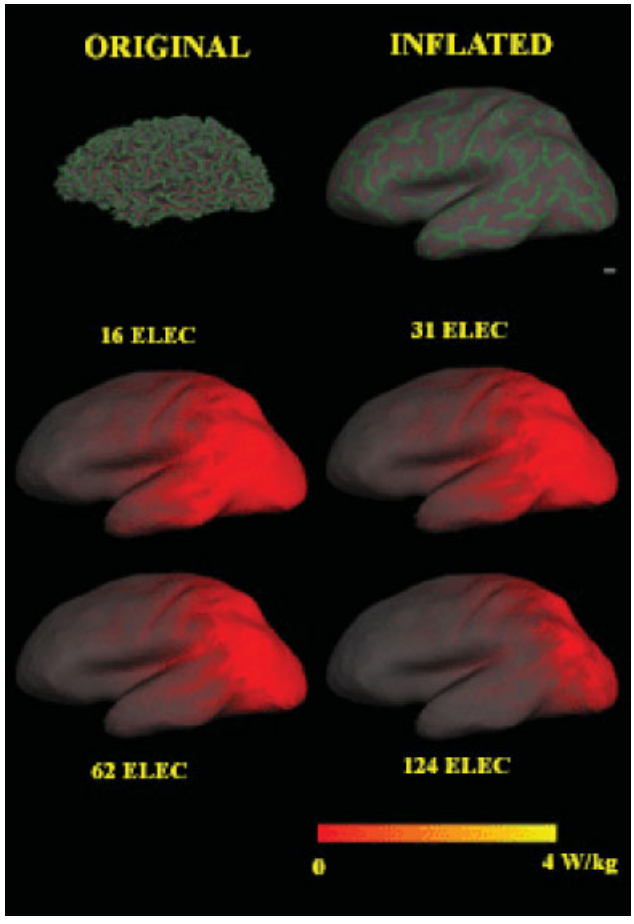

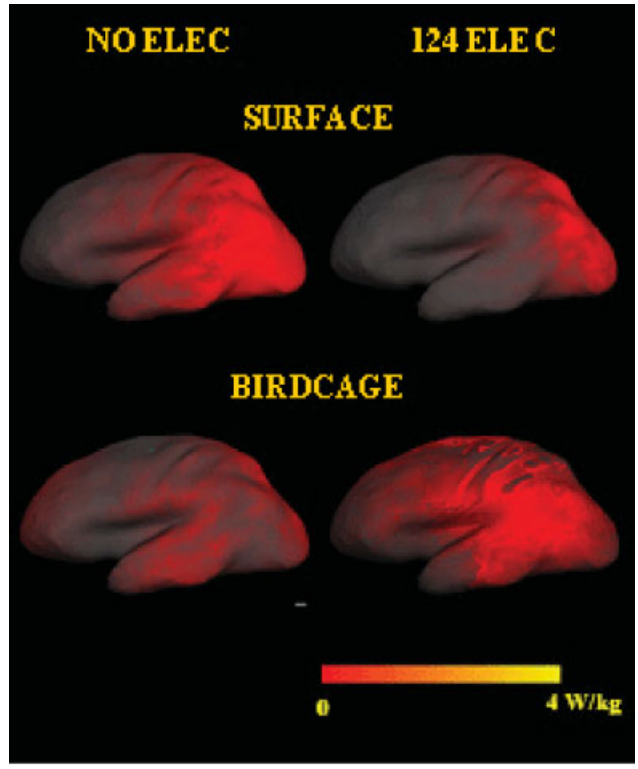

Fig. 5. Overview of computed SAR values shown on the inflated representation of the cortex. The EEG electrode/lead model with surface coil displays the greatest increase of SAR on the posterior part of the cortex. Results are normalized to an input power of 1 W.

the head ($E_{Bcoil} = 86.76$ V/m, $E_{Bhead} = 36.02$ V/m, $E_{Ccoil} = 225.41$ V/m, $E_{Chead} = 19.14$ V/m).

With the electrodes and leads, because of the RF induced currents along the leads, the electric field increases in the proximity of the electrodes/leads ($E_{Acoil} = 80.58$ V/m, $E_{Aelec} = 104.13$ V/m). When the electrodes/leads are added to the head, the change in the electric field associated with the presence of electrodes/leads extends to the distribution of the field around the head. The electrodes/leads increase the electric field on the skin ($E_{Ahead} = 16.38$ V/m, $E_{Ahead+elec} = 586.52$ V/m) and on the surrounding tissues. This generates a higher increase of peak SAR values for both surface and bird cage coils, relative to that produced by the RF of the coil only. In the case of the surface coil, the electric field increases in the posterior part of the head, near the coil ($E_{Chead} = 19.14$ V/m, $E_{Chead+elec} = 24.94$ V/m), and decreases in the anterior part of the head ($E_{Dhead} = 16.39$ V/m, $E_{Dhead+coil} = 11.16$ V/m).

Fig. 4. Top left: Cortical pial representation of original cortex. Top right: Inflated reconstruction of the cortex, with sulci in light green and gyri in dark green. Center and bottom: Local SAR computed with a surface coil and four different EEG montages (16, 31, 62, and 124 electrodes/leads). Results are normalized to an input power of 1 W.

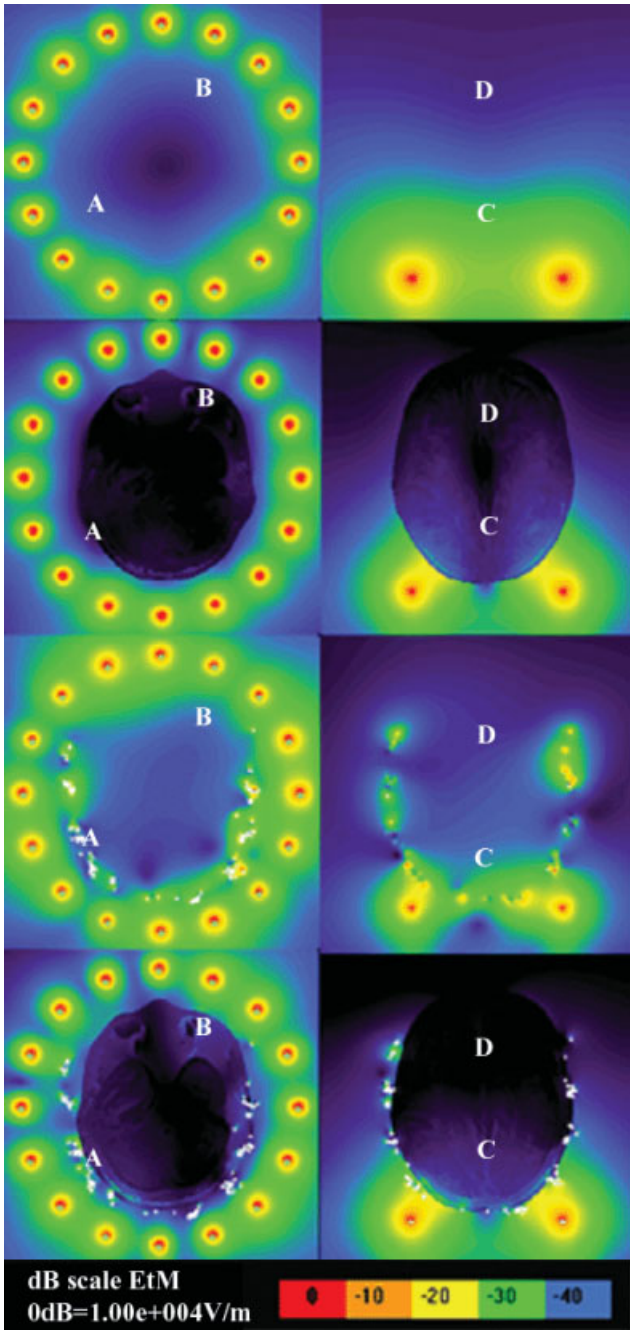

Fig. 6. Electric field distribution with bird cage (left column) and surface (right column) coils in four different cases: coil only (first row), coil plus head (second row), coil plus electrodes/leads (third row), and coil plus head and electrodes/leads (fourth row). We selected four points, two for the bird cage (A, B) and two for the surface (C, D). "A" was in the occipital cortex, "B" was in the eyeball, "C" was selected in the middle of the posterior part of the head, and "D" was in the middle of the anterior part of the head.

Simulations were performed with four different EEG electrodes montages (16, 32, 64, and 128). As shown in Figure 7, there were higher values of SAR on the region close to the electrodes/leads.

Bird Cage Coil

The simulations were performed without and with electrodes/leads (Fig. 8). With the EEG electrode/lead model the peak 1 g averaged SAR level increases by a factor of 172 at 300 MHz and with 124 electrodes/leads (Table 2). For each tissue, the SAR value increases with the number of electrodes/leads (Table 3). In the 124 electrodes/leads case, the neck of the model adjacent to the EEG leads shows an increase of SAR relative to the no-electrodes case. Also, an increase of SAR is visible in the eyes while hot spots are present on the skin (see Table 3 and Figure 8).

Surface Coil

The simulations were performed without and with electrodes/leads (Fig. 9). With the EEG electrode/lead

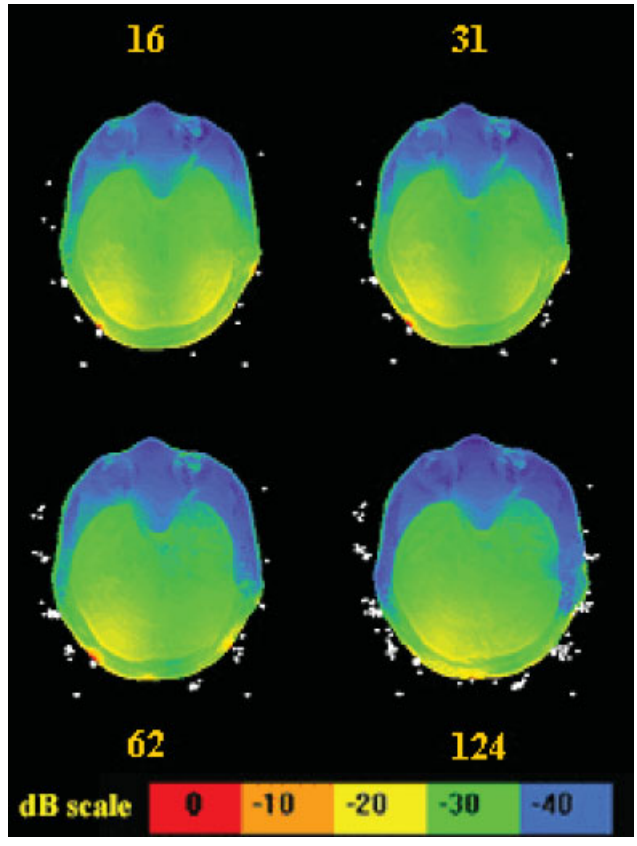

Fig. 7. SAR values obtained using a surface coil and different numbers of electrodes/leads. The SAR value on the skin increases with the number of electrodes/leads. All SAR values are normalized to an input power of 1 W. The scale of the figure is from 0 to −40 dB, 0 dB = 150 W/kg.

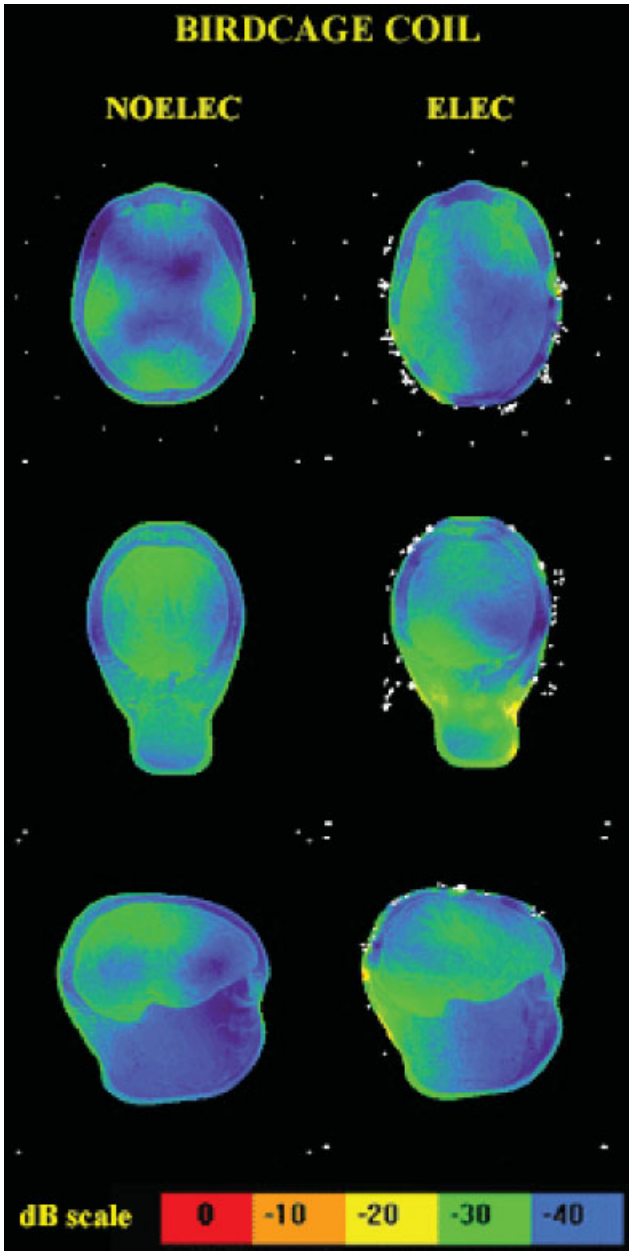

Fig. 8. SAR values computed with the bird cage coil, without (left) and with electrodes/leads. Without electrodes there is a symmetrical distribution of the SAR. All SAR values are normalized to an input power of 1 W. The scale of the figure is from 0 to −40 dB, 0 dB = 150 W/kg.

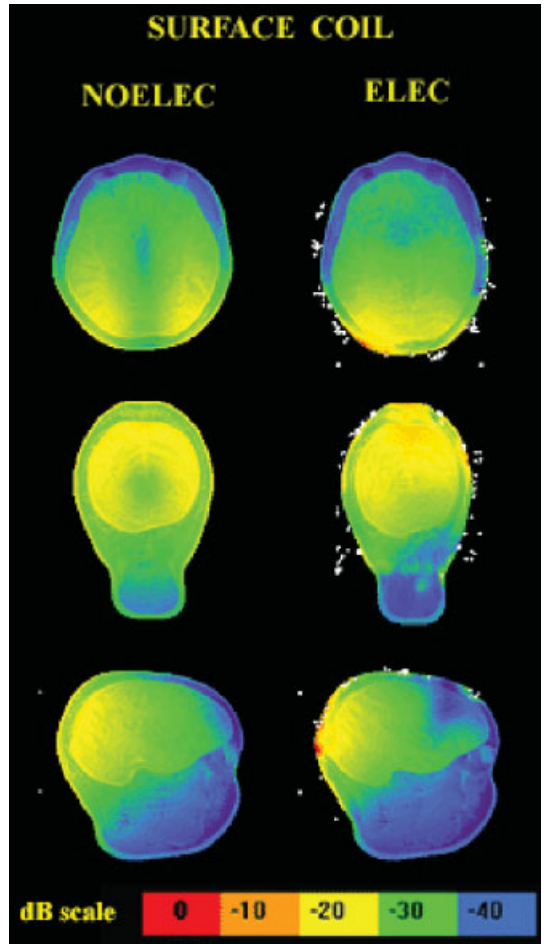

Fig. 9. SAR values obtained with a surface coil, without (left) and with EEG electrodes. Coronal view, second row: Without electrodes, the distribution of the SAR is circularly symmetric. All SAR values are normalized to an input power of 1 W. The scale of the figure is from 0 to −40 dB, 0 dB = 150 W/kg.

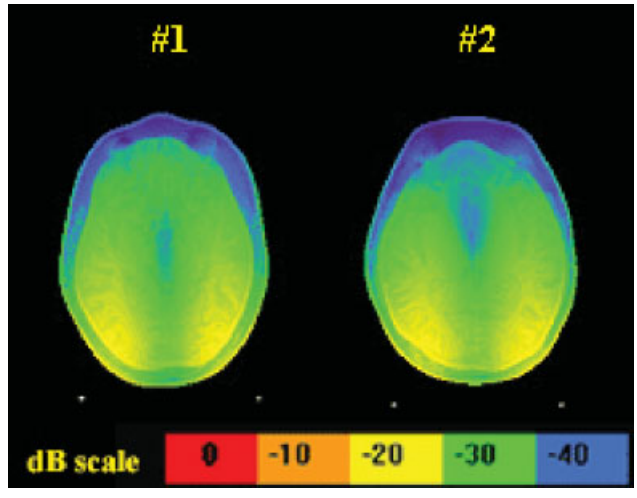

Fig. 10. SAR values computed for both head models with surface coil and no electrodes. The inter-subject variability of the whole head average SAR values is approximately 3%. All SAR values are normalized to an input power of 1 W. The scale of the figure is from 0 to −40 dB, 0 dB = 150 W/kg.

model the peak 1 g averaged SAR level increases by a factor of 15.71 at 128 MHz and with 124 electrodes/leads (Table 2). In particular, the SAR value on the skin increases with the number of electrodes/leads (Table 4). However, in the case of eyes, white and gray matter and whole head SAR, the SAR is greater without electrodes than with electrodes (Table 4). This counterintuitive result is due to the increased asymmetry of the electric field introduced by the EEG electrodes/leads (Figs. 4 and 6). This asymmetry produces a monotonic increase of the ratio between posterior and anterior part of thehead with the number of EEG electrodes/leads (Table 4). SAR was evaluated separately by dividing the volume with a coronal cut (XZ plane, Fig. 3) into two equal sections (each 128 mm long). The ratio between these two values is shown in Table 4 (last row).

Head Models

Our simulations were performed with two head models from two different subjects. As shown in Table 5 and Figure 10, the inter-subject variability of the whole head average SAR values was approximately 3%.

DISCUSSION AND CONCLUSIONS

A growing number of laboratories are employing EEG recordings during fMRI. However, the pulsed RF fields, which are used to elicit MRI signals from tissue, may pose a safety hazard. Here we present results from different simulations, based on the FDTD algorithm. Simulations were performed on high resolution head models generated from MRI data, using different RF coils, numbers of electrodes/leads, and frequencies.

Similar studies have used head models with a lower resolution: $2 \times 2 \times 2.5$ mm^3 [Jin, 1999; Collins and Smith, 2001a]. However, this resolution does not allow us to accurately model very thin tissues, such as bone marrow and skin. These tissues are important due to the proximity of bone marrow and skin to the EEG electrodes. Our high resolution model does not take into account the presence of conductive paste, which is typically placed between electrodes and scalp as an interface. Nevertheless, this model represents the worst case scenario.

Our results confirmed an increase of up to seven times the original value in averaged SAR on the skin, as well as an increase in the tissues adjacent to the electrodes. The study shows that the presence of non-magnetic metallic EEG electrodes/leads can increase the peak 1 g averaged SAR on the subject by as much as 172 times (surface at 300 MHz). Local SAR increases could be partly enhanced due to staircasing effects of dielectric materials [Cangellaris and Wright, 1991; Holland, 1993]. The staircased small structures can perturb the SAR values [Cangellaris and Wright, 1991; Jurgens et al., 1992; Holland, 1993]. Our different models consist of 500 cells (128 MHz) or 1000 cells (300 MHz) per wavelength with a staircase error less than 1 dB [Holland, 1993; Railton and Schneider, 1999]. Furthermore, our findings are consistent with the existing literature [Chou et al., 1996; Ho, 2001].

The FDA guidelines [FDA, 2003] for use in MRI environments recommend SAR levels lower than 3 W/kg averaged over the head for 10 min and 8 W/kg in any gram of tissue in the head for 5 min. In order to comply with this recommendation, the maximum input power should be reduced proportionally to the results in Tables 3–5. For example, when using a surface coil at 300 MHz, the maximum input power for the source considered (sinusoidal) should be reduced by a factor of 16 when using 124 EEG electrodes/leads. This analysis is also applicable to EEG recording during RF exposures to study RF fields (mobile phone use) [Huber et al., 2003].

TABLE 5. Normalized SAR Values Computed for Both Head Models With Input Power of 1 W

Surface no electrodes 300 MHz		
	Subject no. 1 (W/kg)	Subject no. 2 (W/kg)
Whole head	0.236	0.229
Bone and cartilage	0.076	0.050
Skin	0.295	0.257
CSF	0.440	0.433
White matter	0.418	0.406
Gray matter	0.415	0.427
Fat	0.125	0.098
Eyes tissue	0.027	0.016
Bone marrow	0.278	0.236

The inter-subject variability of the whole head SAR is approximately 3%.

ACKNOWLEDGMENTS

We thank Raymond Luebbers and Chris Penney of REMCOM Co. for their kind support and feedback. We thank Jin Kong of M.I.T. and Thomas Vaughan of the CMRR of University of Minnesota for the prolific discussions. We are grateful to Greg Sorensen and Ken Kwong for their supervision during the generation of the model. We also thank Bruce Rosen, Bruce Fischl, Larry Wald, Doug Greve, Jerome Beers, Vitaly Napadow, Evelina Busa, and Patrick Purdon for their collaboration during the development of the project. We are grateful to Gary Boas for the help in the final review process.

REFERENCES

Benar C-G, Gross DW, Wang Y, Petre V, Pike B, Dubeau F, Gotman J. 2002. The BOLD response to interictal epileptiform discharges. Neuroimage 17(3):1182–1192.

Bonmassar G, Schwartz D, Anami K, Belliveau JW, Ives J, Dale A. 1999. Alternative method for recording and analyzing EEG triggered fMRI of interictal spikes. In: 53rd Annual Meeting of the American Epilepsy Society. December 3–9. Orlando, FL.

Bonmassar G, Schwartz DP, Liu AK, Kwong KK, Dale AM, Belliveau JW. 2001. Spatiotemporal brain imaging of visual-evoked activity using interleaved EEG and fMRI recordings. Neuroimage 13(6 Pt 1):1035–1043.

Bonmassar G, Angelone L, Segonne F, Potthast A, Fischl B, Wald L, Belliveau J. 2002. SAR computations in a realistic and high-resolution model of the head with EEG electrodes in place. In: 8th International Conference on Functional Mapping of the Human Brain. June 2–6. Sendai, Japan.

Buchli R, Boesiger P, Meier D. 1988. Heating effects of metallic implants by MRI examinations. Magn Reson Med 7(3):255–261.

Cangellaris AC, Wright SM. 1991. Analysis of the numerical error caused by the stair-stepped approximation of a conducting boundary in FDTD simulations of electromagnetic phenomena. IEEE Trans Antennas Propagation 39: 1518–1525.

Chiappa KH, Hill RA, Huang-Hellinger F, Jenkins BG. 1999. Photosensitive epilepsy studied by functional magnetic resonance imaging and magnetic resonance spectroscopy. Epilepsia 40(Suppl 4):3–7.

Chou CK, Guy AW. 1979. Carbon-loaded teflon electrodes for chronic EEG recordings in microwave research. J Microw Power 14(4):399–404.

Chou CK, McDougall JA, Can KW. 1995. Absence of radio-frequency heating from auditory implants during magnetic resonance imaging. Bioelectromagnetics 16(5):307–316.

Chou CK, Bassen H, Osepchuk J, Balzano Q, Petersen R, Meltz M, Cleveland R, Lin JC, Heynick L. 1996. Radio frequency electromagnetic exposure: Tutorial review on experimental dosimetry. Bioelectromagnetics 17(3):195–208.

Chou CK, McDougall JA, Chan KW. 1997. RF heating of implanted spinal fusion stimulator during magnetic resonance imaging. IEEE Trans Biomed Eng 44(5):367–373.

Christmann C, Ruf M, Braus DF, Flor H. 2002. Simultaneous electroencephalography and functional magnetic resonance imaging of primary and secondary somatosensory cortex in humans after electrical stimulation. Neurosci Lett 333(1): 69–73.

Collins CM, Smith MB. 2001a. Calculations of B(1) distribution, SNR, and SAR for a surface coil adjacent to an anatomically-accurate human body model. Magn Reson Med 45(4):692–699.

Collins CM, Smith MB. 2001b. Signal-to-noise ratio and absorbed power as functions of main magnetic field strength, and definition of ''90 degrees'' RF pulse for the head in the birdcage coil. Magn Reson Med 45(4):684–691.

Dale AM, Sereno MI. 1993. Improved localization of cortical activity by combining EEG and MEG with MRI cortical surface reconstruction: A linear approach. J Cogn Neurosci 5(2):162–176.

Dale AM, Fischl B, Sereno MI. 1999. Cortical surface-based analysis. I. Segmentation and surface reconstruction. Neuroimage 9(2):179–194.

Edwards MB, Taylor KM, Shellock FG. 2000. Prosthetic heart valves: Evaluation of magnetic field interactions, heating, and artifacts at 1.5 T. J Magn Reson Imaging 12(2):363–369.

Fagan LL, Shellock FG, Brenner RJ, Rothman B. 1995. Ex vivo evaluation of ferromagnetism, heating, and artifacts of breast tissue expanders exposed to a 1.5-T MR system. J Magn Reson Imaging 5(5):614–616.

FDA. 2003. Criteria for Significant Risk Investigations of Magnetic Resonance Diagnostic Devices. Center for Devices and Radiological Health. July 14. http://www.fda.gov/cdrh/ode/guidance/793.pdf

Fischl B, Sereno MI, Dale AM. 1999. Cortical surface-based analysis. II: Inflation, flattening, and a surface-based coordinate system. Neuroimage 9(2):195–207.

Freesurfer. 2003. http://surfer.nmr.mgh.harvard.edu

Furse CM, Gandhi OP. 1998. Calculation of electric fields and currents induced in a millimeter-resolution human model at 60 Hz using the FDTD method. Bioelectromagnetics 19(5):293–299.

Gabriel C, Gabriel S, Corthout E. 1996a. The dielectric properties of biological tissues: I. Literature survey. Phys Med Biol 41: 2231–2249.

Gabriel C, Gabriel S, Corthout E. 1996b. The dielectric properties of biological tissues: II. Measurements in the frequency range 10 Hz to 20 GHz. Phys Med Biol 41:2251–2269.

Gabriel C, Gabriel S, Corthout E. 1996c. The dielectric properties of biological tissues: III. Parametric models for the dielectric spectrum of tissues. Phys Med Biol 41:2271–2293.

Gangarosa RE, Minnis JE, Nobbe J, Praschan D, Genberg RW. 1987. Operational safety issues in MRI. Magn Reson Imaging 5(4):287–292.

Gigli F, Fontana M, Brusori S, Capanna R, Smargiassi E, Sartoni Galloni S. 1992. Inherent problems of the use of magnetic resonance in patients with metallic implants currently used in orthopedic practice. Radiol Med (Torino) 83(5):576–584.

Goldman RI, Stern JM, Engel J Jr., Cohen MS. 2000. Acquiring simultaneous EEG and functional MRI. Clin Neurophysiol 111(11):1974–1980.

Hill RA, Chiappa KH, Huang-Hellinger F, Jenkins BG. 1995. EEG during MR imaging: Differentiation of movement artifact from paroxysmal cortical activity. Neurology 45(10):1942–1943.

Ho HS. 2001. Safety of metallic implants in magnetic resonance imaging. J Magn Reson Imaging 14(4):472–477.

Holland R. 1993. Pitfalls of staircase meshing. IEEE Trans Electromagnetics Compatibility 35(4):434–438.

Horovitz SG, Skudlarski P, Gore JC. 2002. Correlations and dissociations between BOLD signal and P300 amplitude in an auditory oddball task: A parametric approach to combining fMRI and ERP. Magn Reson Imaging 20(4):319–325.

Huang-Hellinger FR, Breiter HC, Mc Cormack G, Cohen MS, Kwong KK, Sutton JP, Savoy RL, Weisskoff RM, Davis TL, Baker JR, Belliveau JW, Rosen BR. 1995. Simultaneous functional magnetic resonance imaging and electrophysiological recording. Human Brain Mapp 3:13–23.

Ives JR, Warach S, Schmitt F, Edelman RR, Schomer DL. 1993. Monitoring the patient's EEG during echo planar MRI. Electroencephalogr Clin Neurophysiol 87(6):417–420.

Ives J, Warach S, Patel M, Schlaug G, Edelmen R, Schomer D. 1995. Techniques for monitoring the EEG and triggering functional magnetic resonance imaging scans time-locked to the patient's focal or generalized epileptic discharges. Epilepsia 36(S95).

Jackson GD. 1994. New techniques in magnetic resonance and epilepsy. [Review]. Epilepsia 35(Suppl 6):S2–S13.

Jager L, Werhahn KJ, Hoffmann A, Berthold S, Scholz V, Weber J, Noachtar S, Reiser M. 2002. Focal epileptiform activity in the brain: Detection with spike-related functional MR imaging—preliminary results. Radiology 223(3):860–899.

Jin J-M. 1999. Electromagnetic analysis and design in magnetic resonance imaging. Vol. xiv. Boca Raton: CRC Press. p 282.

Jin JM, Chen J, Chew WC, Gan H, Magin RL, Dimbylow PJ. 1996. Computation of electromagnetic fields for high-frequency magnetic resonance imaging applications. Phys Med Biol 41(12):2719–2738.

Kanal E, Shellock FG, Talagala L. 1990. Safety considerations in MR imaging. Radiology 176(3):593–606.

Kohno K, Back T, Hoehn-Berlage M, Hossmann KA. 1995. A modified rat model of middle cerebral artery thread occlusion under electrophysiological control for magnetic resonance investigations. Magn Reson Imaging 13(1):65–71.

Krakow K, Allen PJ, Lemieux L, Symms MR, Fish DR. 2000. Methodology: EEG-correlated fMRI. Adv Neurol 83:187–201.

Kruggel F, Wiggins CJ, Herrmann CS, von Cramon DY. 2000. Recording of the event-related potentials during functional MRI at 3.0 Tesla field strength. Magn Reson Med 44(2):277–282.

Kruggel F, Herrmann CS, Wiggins CJ, von Cramon DY. 2001. Hemodynamic and electroencephalographic responses to illusory figures: Recording of the evoked potentials during functional MRI. Neuroimage 14(6):1327–1336.

Kunz KS, Luebbers RJ. 1993. The finite difference time domain method for electromagnetics. Boca Raton: CRC Press. p 448.

Lazeyras F, Zimine I, Blanke O, Perrig SH, Seeck M. 2001. Functional MRI with simultaneous EEG recording: Feasibility and application to motor and visual activation. J Magn Reson Imaging 13(6):943–948.

Lemieux L, Allen PJ, Franconi F, Symms MR, Fish DR. 1997. Recording of EEG during fMRI experiments: Patient safety. Magn Reson Med 38(6):943–952.

Lemieux L, Salek-Haddadi A, Josephs O, Allen P, Toms N, Scott C, Krakow K, Turner R, Fish DR. 2001. Event-related fMRI with simultaneous and continuous EEG: Description of the method and initial case report. Neuroimage 14(3):780–787.

Masumoto A, Yonekura S, Haida M, Yanagimachi N, Hotta T. 1997. Analysis of intramedullary cell density by MRI using the multiple spin-echo technique. Am J Hematol 55:134–138.

Matsuda T, Matsuura M, Ohkubo T, Ohkubo H, Atsumi Y, Tamaki M, Takahashi K, Matsushima E, Kojima T. 2002. Influence of arousal level for functional magnetic resonance imaging (fMRI) study: Simultaneous recording of fMRI and electroencephalogram. Psychiatry Clin Neurosci 56(3):289–290.

Moneda AP, Ioannidou MP, Chrissoulidis DP. 2003. Radio-wave exposure of the human head: Analytical study based on a versatile eccentric spheres model including a brain core and a pair of eyeballs. IEEE Trans Biomed Eng 50(6):667–676.

NCRP. 1981. Radiofrequency electromagnetic fields: Properties, quantities, and units, biophysical interaction, and measurement. Bethesda, MD: National Council Radiation Protection and Measurements. Report no. 67.

Nelson DA, Barker ME, Hamlin BH. 1997. Thermal effects of acrylic cementation at bone tumour sites. Int J Hyperthermia 13(3):287–306.

Portas CM, Krakow K, Allen P, Josephs O, Armony JL, Frith CD. 2000. Auditory processing across the sleep-wake cycle: Simultaneous EEG and fMRI monitoring in humans. Neuron 28(3):991–999.

Pruefer D, Kalden P, Schreiber W, Dahm M, Buerke M, Thelen M, Oelert H. 2001. In vitro investigation of prosthetic heart valves in magnetic resonance imaging: Evaluation of potential hazards. J Heart Valve Dis 10(3):410–414.

Railton CJ, Schneider JB. 1999. An analytical and numerical analysis of several locally conformal FDTD schemes. IEEE Trans Microw Theory Tech 47(1):56–66.

Schaefer DJ. 1992. Dosimetry and effects of MR exposure to RF and switched magnetic fields. Ann NY Acad Sci 649:225–236.

Schaefer DJ. 1998. Safety aspects of radiofrequency power deposition in magnetic resonance. Magn Reson Imaging Clin N Am 6(4):775–789.

Schaefer D, Bourland J, Nyenhuis J. 2000. Review of patient safety in time-varying gradient fields. J Magn Reson Imaging 12(1):20–29.

Segonne F, Dale A, Busa E, Glessner M, Salat D, Hahn H, Fischl B. 2001. A hybrid approach to the skull stripping problem in MRI. June 10–14. Brighton, UK.

Shellock FG. 1999. Metallic marking clips used after stereotactic breast biopsy: Ex vivo testing of ferromagnetism, heating, and artifacts associated with MR imaging. AJR Am J Roentgenol 172(5):1417–1419.

Shellock F. 2000. Radiofrequency energy induced heating during procedures: A review. J Magn Reson Imaging 12(1):30–36.

Shellock FG. 2001. Metallic neurosurgical implants: Evaluation of magnetic field interactions, heating, and artifacts at 1.5-Tesla. J Magn Reson Imaging 14(3):295–299.

Shellock FG, Nogueira M, Morisoli S. 1995. MR imaging and vascular access ports: Ex vivo evaluation of ferromagnetism, heating, and artifacts at 1.5 T. J Magn Reson Imaging 5(4): 481–484.

Sijbers J, Michiels I, Verhoye M, Van Audekerke J, Van der Linden A, Van Dyck D. 1999. Restoration of MR-induced artifacts in simultaneously recorded MR/EEG data. Magn Reson Imaging 17(9):1383–1391.

Taflove A, Hagness SC. 2000. Computational electrodynamics: The finite-difference time-domain method. Vol. xxiii. Boston: Artech House. p 852.

Van Audekerkea J, Peeters R, Verhoye M, Sijbers J, Van der Linden A. 2000. Special designed RF-antenna with integrated non-invasive carbon electrodes for simultaneous magnetic resonance imaging and electroencephalography acquisition at 7 T. Magn Reson Imaging 18(7):887–891.

Virtanen J, Rinne T, Ilmoniemi RJ, Naatanen R. 1996. MEG-compatible multichannel EEG electrode array. Electroencephalogr Clin Neurophysiol 99(6):568–570.

Yeung CJ, Susil RC, Atalar E. 2002. RF safety of wires in interventional MRI: Using a safety index. Magn Reson Med 47(1):187–193.

Youssefzadeh S, Baumgartner W, Dorffner R, Gstottner W, Trattnig S. 1998. MR compatibility of Med EL cochlear implants: Clinical testing at 1.0 T. J Comput Assist Tomogr 22(3):346–350.